CrossMark
click for updates

Tuning the thermoelectric properties of A-site deficient SrTiO₃ ceramics by vacancies and carrier concentration

Deepanshu Srivastava,[a] Colin Norman,[a] Feridoon Azough,[a] Marion C. Schäfer,[b] Emmanuel Guilmeau,[b] Demie Kepaptsoglou,[c] Quentin M. Ramasse,[c] Giuseppe Nicotra[d] and Robert Freer*[a]

Ceramics based on $Sr_{0.8}La_{0.067}Ti_{0.8}Nb_{0.2}O_{3-\delta}$ have been prepared by the mixed oxide route. The $La_{1/3}NbO_3$ component generates ~13.4% A-site vacancies; this was fixed for all samples. Powders were sintered under air and reducing conditions at 1450 to 1700 K; products were of high density (>90% theoretical). Processing under reducing conditions led to the formation of a $Ti_{1-x}Nb_xO_{2-y}$ second phase, core–shell structures and oxygen deficiency. X-ray diffraction (XRD) confirmed a simple cubic structure with space group $Pm\bar{3}m$. Transmission electron microscopy revealed a high density of dislocations while analytical scanning transmission electron microscopy at atomic resolution demonstrated a uniform distribution of La, Nb and vacancies in the lattice. X-ray photoemission spectroscopy and thermogravimetry showed the oxygen deficiency (δ value) to be ~0.08 in reduced samples with enhanced carrier concentrations ~2×10^{21} cm^{-3}. Both carrier concentration and carrier mobility increased with sintering time, giving a maximum figure of merit (ZT) of 0.25. Selective additional doping by La or Nb, with no additional A site vacancies, led to the creation of additional carriers and reduced electrical resistivity. Together these led to enhanced ZT values of 0.345 at 1000 K. The contributions from oxygen vacancies and charge carriers have been investigated independently.

Introduction

Thermoelectricity is the basis for a number of efficient techniques to recover energy from waste heat; applications range from radio-isotope thermoelectric generators (RTG) for space missions, to waste heat recovery modules for automotive and industrial environments, and sensors.[1] Candidate materials are screened on the basis of the dimensionless figure of merit ZT (defined as $S^2T/\rho\kappa$, where S is the Seebeck coefficient, ρ is the electrical resistivity, κ is the thermal conductivity and T is the temperature).[2] Traditional thermoelectric materials such as PbTe have been exploited for over 50 years but tend to degrade at high temperatures. In the past two decades there has been growing interest in oxide thermoelectric materials because of their high chemical and thermal stability, and the relative abundance of their constituent species.[3] However, most oxides are intrinsically ionic in nature due to the strong electronegativity

of oxygen, which decreases carrier mobility due to charge localization. Nevertheless, the latter may ultimately improve the Seebeck coefficient.[4] The interaction of charge carriers with the ionic nature of oxide materials and lattice vibrations results in formation of strongly interacting quasi-particles called polarons. These polarons can influence the overall effective mass of the charge carriers in the system by impeding the flow of carriers, which can subsequently enhance the Seebeck coefficient and the process may be further facilitated by creation of oxygen vacancies and nanostructuring as demonstrated in titanates.[5,6]

Instances of high power factor (PF, defined as $S^2\sigma$) were initially recorded in layer-structured materials such as the p-type Na_xCoO_2,[7] and this prompted an investigation of other oxides.[3,8–10] Amongst the perovskite oxides $CaMnO_3$ was one of the first n-type materials investigated in this context, but only a few studies have reported ZT values higher than 0.15.[3,11–13]

$SrTiO_3$ (STO) has now emerged as a leading high temperature n-type oxide thermoelectric.[14] Undoped $SrTiO_3$ has a high Seebeck coefficient ~850 μV K^{-1}, a simple cubic structure,[15] and is relatively easy to dope with aliovalent cations.[16] Lanthanum doping on the A site of $SrTiO_3$ can yield a power factor as high as that of conventional Bi_2Te_3.[17,18] Niobium doping on the B site has raised the high temperature ZT of $SrTiO_3$ to values around 0.35,[19,20]

[a] *School of Materials, University of Manchester, Manchester M13 9PL, UK.*
  E-mail: Robert.Freer@manchester.ac.uk
[b] *Laboratoire CRISMAT, 14050 Caen Cedex, France*
[c] *SuperSTEM Laboratory, SciTech Daresbury Campus, Daresbury WA4 4AD, UK*
[d] *CNR-IMM, Strada VIII, 5, 95121 Catania, Italy*

This journal is © the Owner Societies 2016

Phys. Chem. Chem. Phys., 2016, **18**, 26475–26486 | 26475

due to increases in carrier concentration[14] and effective carrier mass.[21] A number of authors have reported enhanced thermoelectric properties for oxygen-deficient samples.[22,23] However, one of the factors limiting the improvement and practical applicability of $SrTiO_3$-based materials is its high thermal conductivity and its strong temperature dependence,[8] frequently limiting ZT to values <0.2. Thermal transport in $SrTiO_3$ is directly correlated with vacancy concentrations and κ can be substantially lowered by cation substitution and disordered site occupancies.[6,24,25] Neagu and Irvine[26] proposed a mechanism of A-site deficiency to introduce oxygen defects and facilitate further reduction in lattice thermal conductivity (κ_l).

As a result, strontium titanate has been extensively studied in terms of the effects of different additives and processing conditions. Park et al.[27] achieved ZT values above 0.30 at high temperature for La-doped $SrTiO_3$ using colloidal synthesis and spark plasma sintering (SPS), whilst Liu et al.[28] and Kovalevsky et al.[29] obtained more modest values with Dy doping. Simultaneous doping by La and Nb and optimizing the reducing atmosphere yielded ZT values ~0.2 at moderate temperatures.[30,31] Dehkordi et al.[32,33] reported a large improvement in performance with Pr doping of $SrTiO_{3-\delta}$ ($ZT \sim 0.35$) due to the formation of Pr rich grain boundaries and increased carrier mobility. Related investigations of A-site doping employing Pr, Y and Gd were equally successful for power factor and ZT values.[29,34,35] Using pulsed laser deposition, Abutaha et al.[36] fabricated superlattice structures comprising 20 pairs of Pr-doped $SrTiO_{3-\delta}$ (SPTO) and Nb-doped $SrTiO_{3-\delta}$ (STNO) layers, and obtained a very high ZT of 0.46 at 1000 K, improving on the earlier work of Ohta et al.[15] who had previously shown that a superlattice based on $SrTiO_3$: $SrTi_{0.8}Nb_{0.2}O_3$ yielded a ZT of 0.24 at 300 K.

Furthermore, rather than focusing on doping or processing parameters alone, many recent investigations of $SrTiO_3$ have employed multiple strategies to improve properties. Kovalevsky et al.[29,37–39] demonstrated the effect of defect engineering and co-substitutional doping with lanthanide ions (including Dy). Use of highly-reducing sintering conditions generated Ti^{3+}, oxygen vacancies, A-site vacancies and crystallographic shear structures; together these enabled ZT values up to 0.42.[29,40] There is evidence to suggest that an excess number of SrO layers in the $SrTiO_3$ structure decreases overall ZT[41] as resistivity increases faster than the reduction in thermal conductivity. However, the work of Liu et al.[42] and Shoji et al.[43] indicates that a small excess of TiO_2 or TiN in the $SrTiO_3$ matrix, can reduce both thermal conductivity and electrical resistivity. Backhaus-Ricoult et al.[40] also showed the benefits of having inclusions, oxygen vacancies and shear structures within $SrTiO_3$ matrix.

In this investigation we build on our earlier work on La–Nb doped $SrTiO_3$[44] and simultaneously dope STO with lanthanum and niobium, by the incorporation during synthesis of 20 mole% of the A-site deficient perovskite $La_{1/3}NbO_3$. This defines the baseline composition such that approximately 13.34% A site vacancies are created in the final material. The addition of excess La and Nb was utilised to generate additional charge carriers without changing the number of cation vacancies. The aim is therefore to separate the contributions from (i) vacancies

and (ii) excess charge carriers in enhancing thermoelectric properties.

Experimental methods

The starting powders were: $SrCO_3$ (Sigma Aldrich, UK); La_2O_3 (Molycorp Inc, USA); TiO_2 (Sachtleben Chemie GmbH); Nb_2O_5 (Solvay, UK); all had $>99.9\%$ purity. Prior to use, the La_2O_3 was heated at 1173 K for 10 h. The powders were mixed in appropriate molar ratios to produce the $0.8(SrTiO_3)$–$0.2(La_{1/3}NbO_3)$-based samples listed in Table 1.

For each batch of powder, 0.5 mol% excess TiO_2 was added (as a sintering aid), along with equal weights of propan-2-ol and yttria-stabilized zirconia milling balls; batches were vibration milled for 24 h. The resulting slurries were dried, calcined in air at 1373 K, and milled again for 24 h. The final dried powders were passed through a 200 mesh sieve (74 µm) and uniaxially pressed at 90 MPa in a 20 mm diameter hardened steel die to produce cylindrical pellets 5 mm thick. The pellets were placed on 1.5 mm zirconia balls in an alumina crucible and sintered directly in reducing conditions (Ar–5%H_2) in a tube furnace (Vecstar model XF6) at 1450–1750 K for times of 8–48 h, with heating/cooling rate of 180 K h^{-1}.

The densities of the sintered ceramics were determined using the Archimedes method. For phase and microstructural analysis, cross-sections of individual specimens were cut using a diamond wheel, then ground and polished down to 1 µm diamond paste prior to use of a silica suspension (OPS). X-ray diffraction (XRD) was carried out using a Philips X'pert diffractometer with a Cu source. The samples were scanned from 10 degrees to 85 degrees 2θ with a step of size 0.020 degrees and dwell time of 10 s at each step. The XRD spectra were refined using the Rietveld program 'Topas'.[45] Scanning electron microscopy (SEM) was undertaken on a Phillips XL30 FEGSEM, equipped with a Rontec X-ray energy dispersive spectroscopy (EDS) system. Average grain sizes were determined using the linear intercept method.[46]

X-ray photoelectron spectroscopy (XPS) was carried out using a Kratos Axis Ultra instrument with a monochromated Al K$_\alpha$ X-ray source. Samples were polished cross-sections. Detailed scans of electronic transitions of core levels were performed with a resolution of 0.05 eV; data were collected for areas of 700×300 µm. Charge compensation was performed for all samples and peak fitting was carried out using CASAXPS software. The carbon 1s peak at 284.8 eV was used for

Table 1 Formulations of samples $0.8(SrTiO_3)$−$0.2(La_{1/3}NbO_3)$ investigated

$Sr_{0.8}La_{0.067}Ti_{0.8}Nb_{0.2}O_3$	L2	Base composition
$Sr_{0.75}La_{0.11}Ti_{0.8}Nb_{0.2}O_3$	L2-5La	L2 with 5% Sr substituted by La on A-site
$Sr_{0.7}La_{0.16}Ti_{0.8}Nb_{0.2}O_3$	L2-10La	L2 with 10% Sr substituted by La on A-site
$Sr_{0.8}La_{0.067}Ti_{0.75}Nb_{0.25}O_3$	L2-5Nb	L2 with 5% Ti substituted by Nb on B-site
$Sr_{0.8}La_{0.067}Ti_{0.7}Nb_{0.3}O_3$	L2-10Nb	L2 with 10% Ti substituted by Nb on B-site

26476 | *Phys. Chem. Chem. Phys.*, 2016, **18**, 26475–26486

This journal is © the Owner Societies 2016

calibration purposes. Background subtraction from acquired data was carried out using the Shirley approximation. All the characteristic peaks were fitted using the GL30 peak shape, which is a mixture of Gaussian plus 30% Lorentzian.

For thermogravimetric analysis, powdered samples were heated in air up to 1700 K in a Netzsch STA 449 C with heating and cooling rates of 2 K min^{-1}. The sintering behaviour of a pressed pellet of L2 formulation (diameter 10 mm, length 5 mm) was investigated up to 1750 K in air using a dilatometer (Netzsch Model 402 C).

The electrical resistivity (ρ) and Seebeck coefficient (S) of the bulk samples were determined from 300 K to 1050 K using a ZEM-III (Ulvac-Riko). Samples were typically 10 mm × 3 mm × 3 mm in size. Charge carrier concentrations were determined by use of a Physical Property Measurement System (Quantum Design-PPMS) at 400 K. The specimens were typically 2.5 mm × 2.5 mm × 0.3 mm in size.

Thermal diffusivity was determined from 300 K to 1100 K using an in-house laser flash facility.[47] The Cowan method[48] was used to obtain temperature-dependant thermal diffusivity values for all samples. Specific heat capacity was determined by differential scanning calorimetry up to 1000 K (Netzsch STA 449 C).[49] The thermal conductivity (κ) was determined as the product of the physical density, the thermal diffusivity and the heat capacity. The overall figure of merit, ZT was determined from the relationship $ZT = S^2 T/\rho\kappa$. All properties (ρ, S, κ) were determined on the same bulk specimen.

Samples for TEM and STEM investigations were prepared by a conventional crushing technique; sintered disks were crushed into a powder using an agate mortar and pestle. Grains of individual powders were dispersed in chloroform, dropped onto a copper grid covered with a lacey carbon film, and then dried. Structures were initially investigated using selected area electron diffraction (SAED) and high-resolution transmission electron microscopy (HRTEM) techniques using an FEI FEGTEM (Tecnai G2) operating at 300 kV.

Atomic-resolution structural characterization was carried out using a Nion UltraSTEM100 aberration-corrected dedicated STEM, equipped with a Gatan Enfina Spectrometer. The microscope was operated at 100 kV acceleration voltage and the probe-forming optics were configured to form a ~0.9 Å probe (full-width at half-maximum) with a convergence semi-angle of 30 mrad and a probe current of 50 pA. The semi-angular ranges of high angle annular dark field and medium angle annular dark field and annular bright field detectors were 86–190, 40–86 and 15–30 mrad, respectively. The native energy spread of the electron probe was 0.35 eV and the collection semi-angle for the electron energy loss spectroscopy measurements was 36 mrad.

Additional atomic-resolution characterization was carried out using a JEOL ARM200F probe corrected (S)TEM instrument, equipped with a Gatan Quantum spectrometer and a JEOL Centurio EDX spectrometer. The microscope was operated at 200 kV acceleration voltage and the probe-forming optics were configured to form a ~0.8 Å probe (full-width at half-maximum). The semi-angular ranges of high angle annular dark field and annular bright field detectors were 72–290 mrad and 18.7–37.8 mrad, respectively. The native energy spread of the electron probe was 0.35 eV and the collection semi-angle for the Electron Energy Loss spectroscopy (EELS) measurements was 100 mrad.

Scanning distortions in the images were corrected using the Jitterbug[50] plugin for Digital Micrograph (commercially available from HREM Research Inc.). Image simulations were performed using the QSTEM software package, using parameters matching the experimental conditions.[51] Noise in EEL and EDX spectra was removed by Principle Component Analysis using the Cime$^-$ EPFL plugin[52] for Digital Micrograph.

Results and discussion

Microstructure and phase development

Sintering trials of the L2 base material under reducing conditions (Ar–5%H$_2$) showed the optimum temperature to be 1700 K. Detailed studies were carried out at 1700 K for times of 8 h to 48 h. While samples of L2 sintered in air[44] were light grey in colour, the samples sintered in Ar–H$_2$ (this investigation) were black, indicating the presence of Ti^{3+} or oxygen deficiency.[53] All sintered samples were of high density (in excess of 90% theoretical), with density increasing with sintering time (Table 2).

An XRD spectrum of an L2 sample sintered for 24 h is shown in Fig. 1. Topas refinement of all XRD spectra confirmed the cubic $Pm\bar{3}m$ space group for all samples. There were also minor amounts of a rutile (TiO$_2$)-type secondary phase, which increased gradually with sintering time (Table 2). Whilst samples sintered in air contained only the equivalent of the excess TiO$_2$ added as a sintering aid (0.2 wt%), those processed under reducing conditions contained significantly more, up to 4.3 wt%.

Oxygen vacancies were created in the stoichiometric composition L2 by reduction in the sintering atmosphere as shown in the Kroger–Vink equations below.[54] The creation of oxygen vacancies generates free electrons in the system to maintain charge neutrality while O$_2$ gas reacts with H$_2$ to form steam:
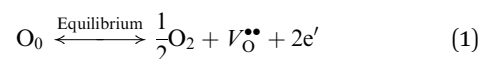
$$O_0 \xrightleftharpoons[\text{}]{\text{Equilibrium}} \frac{1}{2}O_2 + V_O^{\bullet\bullet} + 2e' \qquad (1)$$

Table 2 Lattice parameters and densities for L2 specimens

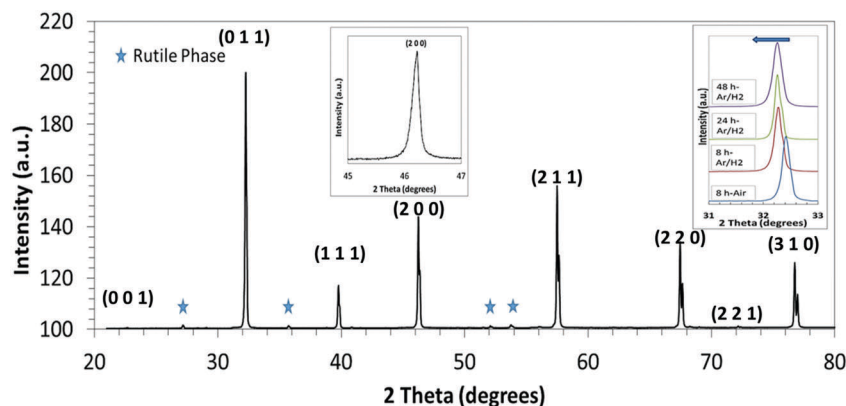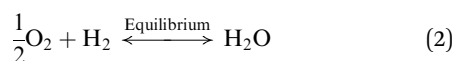| Sintering conditions	Lattice parameter (Å ± 0.001)	Rutile structured phase (±0.1 wt%)	Density (±0.025 g cm^{-3})	Relative density (±0.5%)
Air-8 hour	3.913	0.2	4.850	94.4
Ar–H$_2$-8 hour	3.919	2.6	4.693	91.3
Ar–H$_2$-24 hour	3.923	3.3	4.915	95.5
Ar–H$_2$-48 hour	3.924	4.3	5.033	97.2

Fig. 1 XRD spectrum of the L2 sample sintered in Ar–H$_2$ for 24 h; inset (1) shows details of the (200) peak; inset (2) shows the lateral movement in the (011) peaks for samples sintered for different times. The peaks marked with a star represent a rutile-structured secondary phase.

$$\frac{1}{2}O_2 + H_2 \xleftrightarrow{\text{Equilibrium}} H_2O \qquad (2)$$

With increasing sintering time under reducing conditions, the XRD diffraction peaks move to lower diffraction angles, reflecting a small overall increase ($\sim 0.3\%$) in the lattice parameter as shown in Table 2. The larger lattice parameter can be explained by the formation of Ti^{3+}/Nb^{4+} to compensate excess electrons from oxygen vacancies created during sintering under reducing atmosphere of Ar/5%H$_2$. The cations Ti^{3+}/Nb^{4+} have larger ionic radii than Ti^{4+}/Nb^{5+} in the TiO$_6$ octahedra and help to increase the unit cell volume. These changes in lattice parameters are in agreement with published work on perovskite materials sintered in different environments.[55,56]

The evolution of the microstructure is presented in Fig. 2. All L2 specimens exhibit regular polygonal grains, with size increasing with sintering time under reducing conditions; from 7 μm for a time of 8 h (Fig. 2b) to 10 μm for 24 h (Fig. 2c), to 12 μm for 48 h. In contrast, samples sintered for only 8 h in air achieved grain sizes of typically 13 μm (Fig. 2a). Higher magnification, backscattered images of L2 samples sintered in Ar–5%H$_2$ for 24 hours revealed the presence of core–shell structures (Fig. 2d); EDS analysis and mapping indicated that the cores are rich in La and Nb. Detailed analysis indicated that the atomic ratio of Nb:Ti in the core regions is $\sim 1:2.8$ compared to the stoichiometric ratio of $1:4$ in shell regions. The La:Sr ratio was found to be as high as $1:3.5$ in the core regions but up to $\sim 1:12$ in the shell regions. The La:Sr/Nb:Ti ratios changed with sintering time under reducing conditions; the core regions were richer in La/Nb in the 24 h samples than in the 48 h samples. These core–shell structures were present in all samples sintered in reducing conditions. When samples were sintered in air for periods up to 24 h, there was very little evidence of La/Nb-rich cores. This suggests that the cores may be the result of an intermediary phase from the calcination process, which is stable in samples sintered in reducing conditions. No additional phases were identified in the calcined powders.
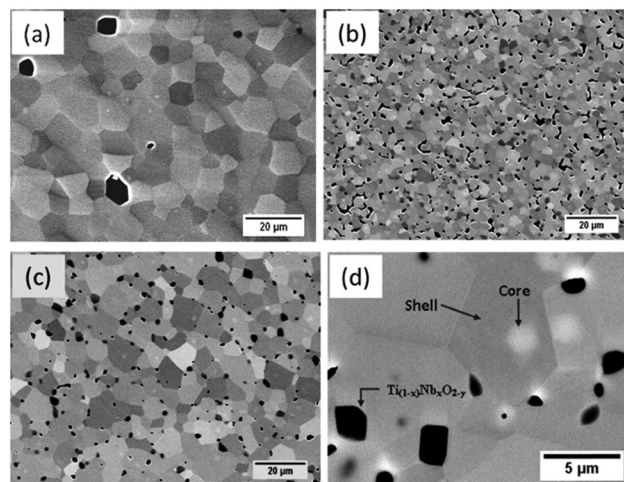

Fig. 2 Secondary electron images of L2 samples: (a) sintered in air for 8 h, (b) sintered in Ar–5%H$_2$ for 8 h, and (c) sintered in Ar–H$_2$ for 24 h. (d) backscattered image of the L2 sample sintered in Ar–5%H$_2$ for 24 hours.

Another significant feature in the microstructures of samples sintered under reducing conditions was a TiO$_2$-based secondary phase. This was first identified in XRD spectra (Fig. 1) and is visible in SEM micrographs as rectangular to rounded black regions typically 1–2 μm in size (Fig. 2d). The total amount and size of individual regions increased with sintering time. Detailed EDS analysis indicated that these regions are Ti–Nb rich oxides; in samples sintered for 48 hours the Ti:Nb ratio was 10:3. It is proposed that as increasing concentrations of oxygen vacancies are created in the matrix, these Ti$_{(1-x)}$Nb$_x$O$_{2-y}$ based secondary phases are precipitated, mainly at grain boundaries.

Electron microscopy

On a representative example of the samples sintered under reducing conditions, detailed electron microscopy was undertaken on L2 ceramics sintered in Ar–5%H$_2$ for 24 hours. For convenience these samples will be referred to as L2ArH-24h for the remainder of this discussion. A conventional bright field TEM image for L2ArH-24h is shown in Fig. 3a. A high density of
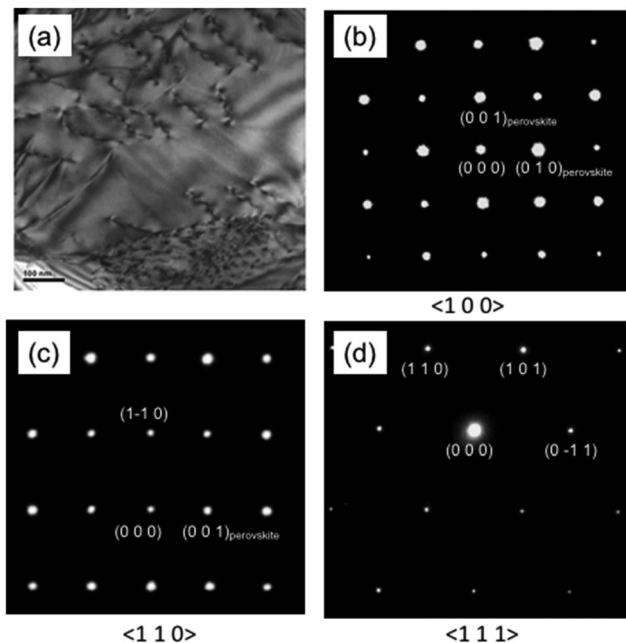
26478 | *Phys. Chem. Chem. Phys.*, 2016, **18**, 26475–26486

This journal is © the Owner Societies 2016

Fig. 3 (a) TEM image for the L2-Ar/H$_2$-24h sample. Selected area electron diffraction patterns for major zone axes for the L2-Ar/H$_2$-24h sample along the ⟨100⟩ (c) ⟨110⟩ and (d) ⟨111⟩ zone axes.

dislocations is visible. The presence of dislocations is common in air-sintered, un-doped SrTiO$_3$ ceramics.[57,58] However, we are not aware of any reports documenting the presence of dislocations in Ln (La, Nd, Pr) doped or Nb-doped SrTiO$_3$ based ceramics exhibiting good thermoelectric properties and high *ZT* values.

To confirm the simple cubic structure deduced from XRD investigation, electron diffraction patterns from three major zone axes were collected (Fig. 3b–d). The diffraction patterns can be indexed as simple cubic symmetry. No extra or diffuse reflections that would suggest the presence of oxygen octahedral tilting, long range or short range ordering can be seen in the diffraction patterns.

To provide further insight into the nature of the reduced Sr$_{0.8}$La$_{0.067}$Ti$_{0.8}$Nb$_{0.2}$O$_3$ ceramics, an investigation of the atomic structure and chemistry of L2ArH-24h was performed using atomically resolved STEM imaging and EELS measurements.

Fig. 4 shows HAADF STEM images (averaged through rigid registration of a stack of 30 consecutive frames acquired in quick succession) of the L2ArH-24h sample acquired along the [100] and [110] zone axes, respectively. The intensity of A and B sites, observed in the chemically-sensitive Z contrast HAADF images,[59] is relatively uniform suggesting a random cation and vacancy distribution throughout the sample. Small site-to-site intensity variations, while present, do not appear to possess any short- to medium-range order, as also evidenced by the absence of additional reflections in the Fourier transform of these images (insets in Fig. 4a and b). Furthermore, no phase separation, defects or other structural domains were observed in the images. As HAADF images are mostly sensitive to heavier elements, often making O columns impossible to distinguish, we have performed Annular Bright Field (ABF) imaging, an imaging mode sensitive to both light and heavy columns allowing for direct imaging of the oxygen positions in the lattice;[60] in this imaging mode the atomic positions appear dark on a white background. A representative ABF image (averaged by rigid-registration of 30 consecutive frames acquired in fast succession) acquired along the [110] zone axis of the L2ArH-24h sample is shown in Fig. 4c. In this orientation the B-site (Nb, Ti) columns are separated from both the A-site cations as well as the O columns (see the ball and stick inset in Fig. 4c), which allows for a direct observation of the BO$_6$ octahedral units, and the detection of possible octahedral tilts or distortions of the O sub-lattice. An image simulation using a structural model with *Pm3̄m* symmetry is overlaid on the image bottom-right corner, showing a good qualitative agreement (in particular for the O column positions). Furthermore, as for the HAADF images, the Fourier transform of the ABF image (inset Fig. 4c) does not reveal any superlattice or long range order reflections. These atomic-scale results thus confirm the findings from XRD and SAED (Fig. 4) that the structure adopts a *Pm3̄m* symmetry.

In order to confirm the absence of any chemical ordering in the sample we employed atomically-resolved chemical mapping through simultaneous EDX and EEL spectrum imaging.
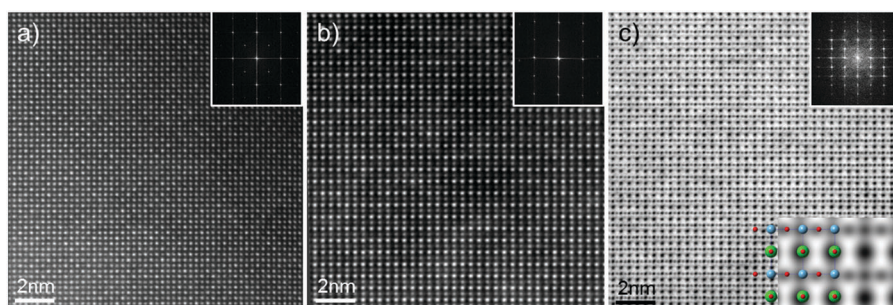

Fig. 4 HAADF STEM images and corresponding Fourier transforms (insets) of the L2ArH-24h sample acquired along the [100] (a) and [110] (b) zone axes, respectively. In (a) the atomic columns in the diagonal directions represent the lattice directions of the cubic structure. (c) Annular Bright Field STEM image of the same sample acquired along the [110] axis. The inset in the bottom-right corner corresponds to a simulated ABF image using the *Pm3̄m* crystal structure, with overlaid ball and stick model of the *Pm3̄m* structure, where the colour assignment is as follows: A-site, green; B-site; blue and O-site, red.

This journal is © the Owner Societies 2016

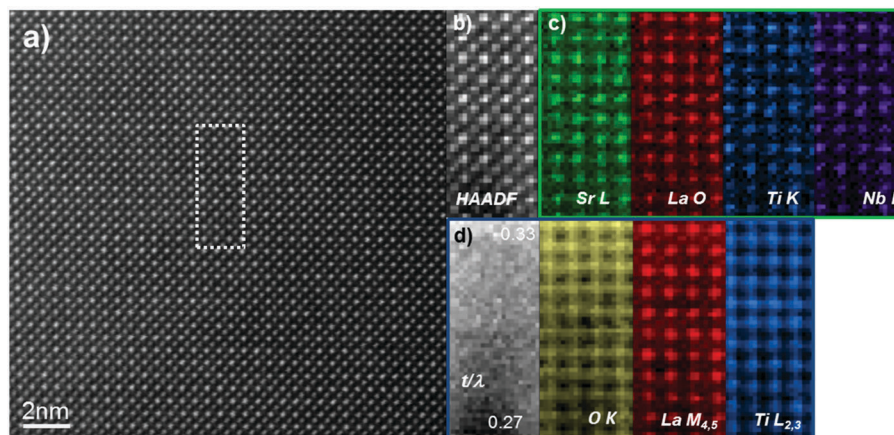*Phys. Chem. Chem. Phys.*, 2016, **18**, 26475–26486 | 26479

Fig. 5 (a) HAADF STEM image of the L2ArH-24h sample, acquired along the [100] zone axis, showing the area used for analysis. (b) HAADF signal acquired simultaneously with (c) EDXS and (d) EELS data. The resulting chemical maps show a highly-uniform distribution of the constituent elements in the lattice. A relative thickness map in (d) (t/λ), (where λ is the inelastic mean free path of the electrons within the material) was also computed, in order to eliminate any possible misinterpretation due to thickness variations within the field of view.

Chemical maps were acquired by rastering the electron probe serially across a defined region and simultaneously collecting EELS and EDX spectra at each point. EDX elemental maps were created by integrating, at each point of the spectrum images, the peak intensity of the Sr L, La O, Nb L and Ti K characteristic X-ray peaks. Similarly, EELS elemental maps were created by integrating at each point of the corresponding spectrum images the spectrum intensity over a ~ 40 eV window above the Ti $L_{2,3}$, and La $M_{4,5}$ EELS edge onsets after background subtraction using a power law model. Fig. 5 shows representative data collected along the [100] direction for the L2ArH-24h sample; the data indicates that both A-site dopants (La and vacancies) and the B-site dopant (Nb) are uniformly distributed throughout the lattice. There is no evidence of any form of cation or vacancy ordering within the field-of-view studied here; additional datasets were acquired throughout the sample with the same conclusions.

Oxygen deficiency and cation valence state

X-ray photoelectron spectroscopy. XPS data were collected for the four types of L2 sample; characteristic doublet peaks for Ti and Nb are presented in Fig. 6. The dominant Ti 2p doublet peaks at approximately 458.4 eV and 464.1 eV (Fig. 6a) can be attributed to Ti $2p_{3/2}$ and Ti $2p_{1/2}$. The doublet separation of 5.72 eV indicates the major oxidation state was Ti^{4+}.[61,62] The second set of doublet peaks corresponds to the oxidation state of Ti^{3+}. The relative fraction of Ti^{3+}/Ti^{4+} in the L2 samples is given in Table 3. In the reduced samples the fraction of Ti^{3+} to total Ti (*i.e.* Ti^{4+} + Ti^{3+}) was as high as 10–12%, compared to less than 2% for air-sintered samples (data in the inset of Fig. 6a). The latter may correspond to disorder in the lattice and the presence of oxygen vacancies.

Similarly, the XPS data for the L2 samples could be deconvoluted to yield peaks for oxidation states of 4+ and 5+ for Nb 3d.
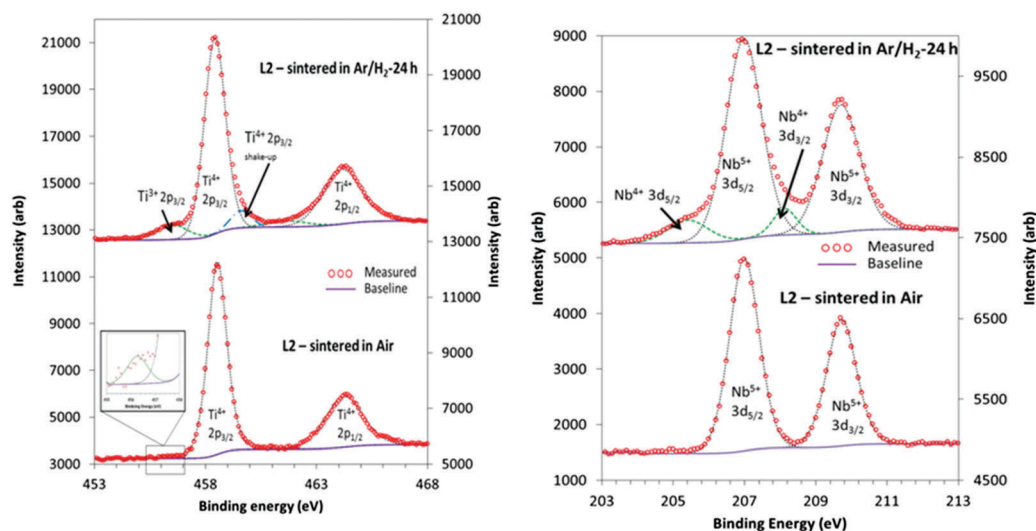

Fig. 6 XPS Characteristic doublet peaks obtained for Ti 2p (left) and Nb 3d (right) for L2 samples sintered in air for 8 hours and reducing conditions for 24 hours.

26480 | *Phys. Chem. Chem. Phys.*, 2016, **18**, 26475–26486

This journal is © the Owner Societies 2016

Table 3 Relative Fractions of Ti^{3+} and Nb^{4+} in sintered samples; numbers in parentheses indicate uncertainties

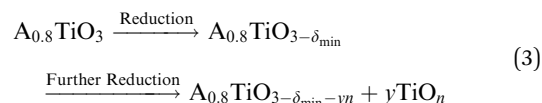| Sample	L2 Air	L2ArH-8h	L2ArH-24h	L2ArH-48h
%Ti^{3+}/total Ti	1.6 (1)	8.6 (4)	10.2 (5)	11.5 (5)
%Nb^{4+}/total Nb	0	11.0 (5)	10.4 (5)	10.8 (5)

Fig. 6b shows the $3d_{5/2}$ and $3d_{3/2}$ doublet, with peak positions of 206.9 eV and 209.7 eV, and a separation of 2.7 eV. In most of the reduced samples the amount of Nb^{4+} as a fraction of total Nb was typically 11% (Table 3), whilst there was no Nb^{4+} in the air-sintered samples. In general, samples sintered in reducing conditions exhibited a higher concentration of Ti^{3+} than Nb^{4+} oxidation states, and the fraction of Ti^{3+} increased with sintering time.

Thermogravimetric analysis. In order to determine the degree of oxygen deficiency (δ) in the samples sintered under reducing conditions, they were subjected to thermogravimetric analysis in air. Upon heating the samples started to gain weight around 400–500 °C, but there was minimal weight gain beyond 850 °C. There was no significant weight change on cooling. By assuming that the final product after cooling was fully oxidised, the oxygen deficiency for samples sintered under reducing conditions for 24 hours was calculated to be equivalent to a δ value of 0.082. This corresponds to a (Ti^{3+}/total Ti) plus (Nb^{4+}/total Nb) ratio of 20%, which is very close to the sum of individual fractions determined by XPS (Table 3). The important point is that there is a significant contribution to the oxygen vacancy concentration from the reduction of Nb as well as Ti; the former has been largely ignored in a number of earlier studies.[38,63] However, the increase in Ti^{3+} (and to a lesser extent Nb^{4+}) with increased reduction of the samples (revealed by both XPS and thermogravimetry) should correlate with the increased carrier concentration and hence improved thermoelectric properties.

Thermoelectric properties. The air-sintered samples exhibited high electrical resistivity and poor thermoelectric properties, consistent with earlier studies.[44] Consequently, this discussion focusses on the samples sintered under reducing conditions. With increased sintering time, both the electrical resistivity and Seebeck coefficients reduced systematically (Fig. 7). This decrease can be attributed to an increase in carrier concentration, brought about by the reduction process. The transition temperature for semiconductor to metallic behaviour reduced with increasing sintering time (from 500 K for 8 hours) to room temperature for samples sintered for 48 hours. The Seebeck coefficient decreased with increasing sintering time, and the increased degree of reduction (Fig. 7b); this is partially compensated by the effect of improved electrical conductivity (Fig. 7a). However, the thermal conductivity increased slightly with increased sintering time (Fig. 7c).

In Fig. 2, the concentration of microstructural defects in L2 sample was observed to change with increase in sintering time. The density of the samples and the quantity of secondary phase segregation of $(Ti,Nb)O_{2-x}$ increased with sintering time (Table 2), while the change in core–shell structure with time was insignificant. This increase in density is related to increase

in effective diffusion distance during sintering, which is proportional to the square root of sintering time ($\propto \sqrt{t_{dwell}}$).[64] On the other hand, the increasing reduction of $SrTiO_3$ based samples in Ar/H_2 results in increasing segregation of TiO_{2-y} phase at grain boundaries and triple point junctions. Irvine et al.[65] showed that sintering A-site deficient titanates in a reducing atmosphere exsolves TiO_2 after an oxygen deficiency limit (δ_{min}) is reached, as shown in eqn (3):

$$A_{0.8}TiO_3 \xrightarrow{\text{Reduction}} A_{0.8}TiO_{3-\delta_{min}}$$
$$\xrightarrow{\text{Further Reduction}} A_{0.8}TiO_{3-\delta_{min}-yn} + yTiO_n \tag{3}$$

The thermal conductivity of the samples will be affected by the presence of these defects. While, the increase in the density generally increases the overall thermal conductivity, the effect of non-stoichiometric phase segregations is proposed to reduce the overall thermal conductivity by creating more scattering centres due to difference in crystal structures. However, the most prominent improvement comes from optimized A-site vacancy concentrations, as observed in our earlier investigation.[44]

The baseline L2 samples contain 13.3% A site vacancies,[44] which are maintained in oxidised and reduced samples. In addition, the oxygen vacancies, grain boundaries, second phases and distributed core–shell structures will also contribute to phonon scattering and help to improve thermoelectric performance. In general, thermal conductivity was at least 10–12% lower for samples with core–shell structures than for the samples without them. Collectively, the various structural defects can help reduce the lattice thermal conductivity κ_l.

The grain sizes for the L2 samples sintered in Ar/H_2 increased from 7–12 μm with increase in sintering time. This variation should modify the volume of grain boundary interface regions and the scattering centres in the bulk specimen, and possibly affect thermal conductivity. However, the grain sizes for the L2 samples are relatively large (several microns) and the variation modest. Koumoto et al.[8] demonstrated that grain size changes only had a significant effect on thermal conductivity when grain sizes were in the range of few tens of nanometres. This is also supported by the fact that the temperature-dependent average phonon mean paths in $SrTiO_3$ based materials of the order of 1–2 nm and not significantly affected by the grain sizes of order of microns.

The total thermal conductivity is the sum of the lattice and electronic thermal conductivity. The electronic thermal conductivity[8] κ_e is given by:

$$\kappa_e = L_0 T \sigma \tag{4}$$

where L_0 is the Lorenz factor and σ is the electrical conductivity of the sample at temperature T. The calculated values of κ_e at 1000 K for L2 samples sintered for 8, 24 and 48 hours are 0.26, 0.46 and 0.87 W m^{-1} K^{-1} respectively. It is noted that for samples sintered for 8 hours, the electronic thermal conductivity represented a small fraction of total κ, amounting to approximately 10%, whilst for samples sintered for 48 hours, the κ_e value was a significant fraction, around 25% of the total κ. Since, the

This journal is © the Owner Societies 2016

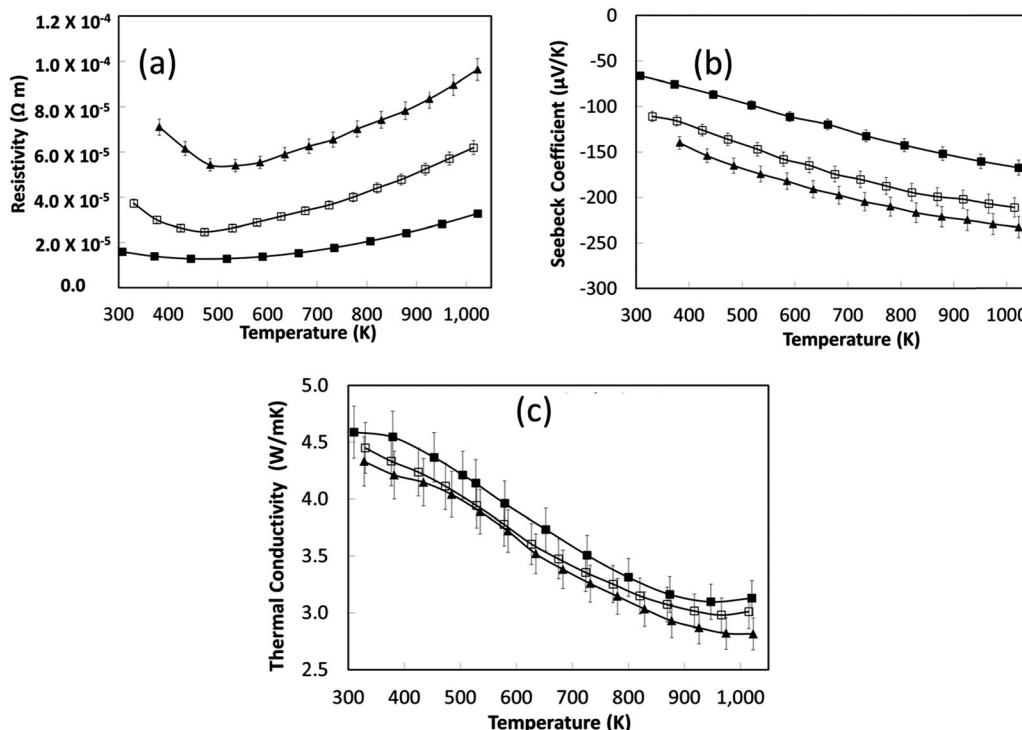*Phys. Chem. Chem. Phys.,* 2016, **18**, 26475–26486 | **26481**

Fig. 7 Temperature dependence of (a) the electrical resistivity, (b) the Seebeck coefficient and (c) the total thermal conductivity for L2 samples sintered under reducing conditions. The legend key is as follows: L2-(Ar/H$_2$)-8 hours is represented by closed triangle (▲); L2-(Ar/H$_2$)-24 hours is represented by open square (□); L2-(Ar/H$_2$)-48 hours is represented by closed square (■).

change in total κ was modest (Fig. 7c), while κ_e increased steeply with an increase in sintering time, it can be deduced that κ_l is reduced significantly (by $\sim$20%) as the sintering time is increased from 8 to 48 hours. This is attributed to the increased oxygen vacancies and the microstructural differences.

The small increase in total κ with increased sintering time is again associated with an increase in carrier concentration. Nevertheless, the total thermal conductivity of the reduced samples (Fig. 7c) is significantly less than for air-sintered samples, typically 12 W m^{-1} K^{-1} at room temperature to 5 W m^{-1} K^{-1} at 1000 K.[66] Disordering of A-site vacancies remains a dominant factor for the thermal conductivity reduction.

Charge carrier concentrations for the L2 samples were determined experimentally and calculated via the modified Hiekes' equation:[67]

$$n = \left[\frac{A_s}{V}\right]\left[\frac{1}{e^{(S \times e/(k_B))} + 1}\right] \tag{5}$$

where $\frac{A_s}{V}$ is the number of available sites per unit volume of unit cell; for the cubic peroskite structure A_s is 1 and the cell constant is $\cong 0.3905$ nm. The quantity $((k_B)/e)$ is the ratio of the Boltzmann constant to the electronic charge and is approximately equal to 87 μV K^{-1}; S is the Seebeck coefficient. The use of Hiekes formula assumes negligible spin orbit degeneracy and configurational entropy contributions to thermopower[67] and is used here only to determine the approximate levels of carrier concentration. More detailed understanding of material

dependant properties and use of Mott's formula might be more suitable to estimate well correlated values of carrier concentration compared to calculated values obtained by the Hall measurements. The collected data (Table 4) show that carrier concentrations in the L2 samples are approximately 4×10^{21} cm^{-3} and increased with sintering time and the increasing degree of reduction. In contrast, carrier concentrations in air-sintered samples are typically three orders of magnitude lower.

To provide further insight into the nature of the samples, charge mobility and effective mass values were calculated. The charge mobility (μ) was obtained via the standard conductivity relationship, eqn (6):

$$\sigma = ne\mu \tag{6}$$

where σ is the electrical conductivity, n the carrier concentration, and e the electronic charge. Effective mass values were deduced via the relationship linking the Seebeck coefficient and $\left(\frac{m^*}{n^{\frac{2}{3}}}\right)$ as shown by eqn (7):[56,68]

$$S = \left(\frac{8\pi^2 k^2}{3eh^2}\right)(Tm^*)\left(\frac{\pi}{3n}\right)^{\frac{2}{3}}(1+r) \tag{7}$$

where h is the Planck constant, m^* is the effective mass, n is the carrier concentration and r is the scattering parameter, which is assumed to be 0.5 for ionic solids.[69] Uncertainties in carrier mass values are $\sim$10%. Whilst charge mobility increased with increasing levels of sample reduction (Table 4), the effective

26482 | *Phys. Chem. Chem. Phys.*, 2016, **18**, 26475–26486

This journal is © the Owner Societies 2016

Table 4 Carrier concentration, mobility and carrier mass for L2 samples sintered under different conditions

Sintering conditions	Carrier concentration (cm^{-3}) ($\pm 10\%$)		Charge mobility ($cm^2 \, V^{-1} \, s^{-1}$)	m^*/m_0	$m^*/n^{2/3}$ ($10^{-14} \, cm^2$)
	Calculated	Experimental			
Air-8 hour	1.58×10^{18}		0.79	0.273	$0.199 \, m_0$
Ar–H_2-8 hour	1.02×10^{21}		0.86	3.84	$3.727 \, m_0$
Ar–H_2-24 hour	4.19×10^{21}	1.69×10^{21}	1.34	4.30	$2.98 \, m_0$
Ar–H_2-48 hour	6.67×10^{21}	2.83×10^{21}	1.64	4.04	$1.987 \, m_0$

carrier mass increased to maximum value of 4.3 after 24 hours, suggesting that 24 hours could be the optimum sintering time. The carrier concentrations reported here are in broad agreement with values reported for heavily doped SrTiO$_3$ ceramics, while the mobility values are almost an order lower than for similar oxides.[23,56]

Based on the thermoelectric parameters presented in Fig. 7, the thermoelectric figure of merit (*ZT*) was determined (Fig. 8). With increasing sintering time under reducing conditions there was a steady increase in *ZT* to a maximum value of 0.27 at 1000 K; samples sintered for 8 hours had a peak *ZT* of 0.2. This demonstrates the importance of the reducing environments for processing SrTiO$_3$-based materials; the same materials sintered in air attained a maximum *ZT* value of 0.004 at 1000 K.[44] The improvement in *ZT* with increased sintering time under reducing conditions can be linked directly to the steady increase in carrier concentration with sintering time (Table 4). However, carrier mobility did not improve by the same degree suggesting strong scattering of carriers within the bulk material.

With the control of the processing environment, the composition, the carrier concentration and the effective TE properties can be optimised and improved significantly. So far we have focussed on the effect of changing δ, and therefore the oxygen vacancy concentration, whilst the A site vacancy concentration was fixed. Having now optimised processing conditions for Sr$_{0.8}$La$_{0.067}$Ti$_{0.8}$Nb$_{0.2}$O$_3$ we maintain the A-site vacancy concentration, but vary the number of excess charge carriers through doping on the A and B sites, to separately define the contribution of excess carriers.
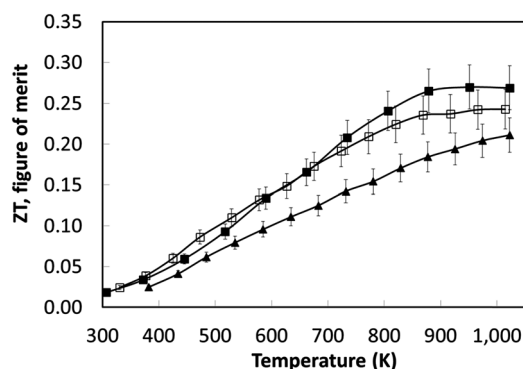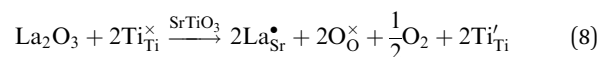

Fig. 8 Temperature dependence of the thermoelectric figure of merit for L2 samples sintered under reducing conditions. The legend key is as follows: L2-(Ar/H$_2$)-8 hours is represented by closed triangle (▲); L2-(Ar/H$_2$)-24 hours is represented by open square (□); L2-(Ar/H$_2$)-48 hours is represented by closed square (■).
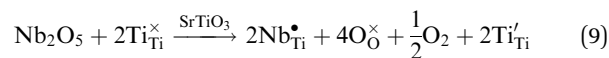
Effect of excess La/Nb substitution in Sr$_{0.8}$La$_{0.067}$Ti$_{0.8}$Nb$_{0.2}$O$_{3-\delta}$. In view of the clear benefit of processing SrTiO$_3$-based ceramics under reducing conditions, we attempted to further improve the thermoelectric properties by generating additional charge carriers through substitution of excess lanthanum and niobium, on A and B sites respectively, without creating further cation vacancies. Four separate formulations, with either 5 or 10% excess La or Nb were prepared; the total number of cations on each site was kept constant, *i.e.* 0.867 on the A site and 1.000 on the B site as in the L2 composition (Table 1).

Lanthanum doping of SrTiO$_3$ on the A site increases the number of charge carriers and generates surplus electrons. The latter are charge-compensated by reduction of Ti from 4+ to 3+. These changes can be represented by the following Kröger–Vink equations, which has been discussed in detail by Koumoto *et al.*[8] These effects are independent of the reduction that occurs during sintering, which also gives rise to additional charge carriers.

$$La_2O_3 + 2Ti_{Ti}^{\times} \xrightarrow{SrTiO_3} 2La_{Sr}^{\bullet} + 2O_O^{\times} + \frac{1}{2}O_2 + 2Ti_{Ti}' \quad (8)$$

Similarly, niobium doping on the B sites generates both Nb^{4+} and Ti^{3+} in the bulk.

$$Nb_2O_5 + 2Ti_{Ti}^{\times} \xrightarrow{SrTiO_3} 2Nb_{Ti}^{\bullet} + 4O_O^{\times} + \frac{1}{2}O_2 + 2Ti_{Ti}' \quad (9)$$

All four formulations (Table 1) were sintered under reducing conditions for 24 hours, with a baseline standard L2 sample used as a control. Sintered densities of all the samples prepared with either excess La or Nb were at least 95% theoretical. Typical microstructures are shown in Fig. 9. The main features are very similar to those shown in Fig. 2, but the grain sizes were smaller than the L2 control sample by approximately 50% (Fig. 2c and d). Grain size dependence on thermal conductivity is considered to be effective for grain sizes in the nanoscale range. The Ti–Nb rich secondary phases are evident in the back-scattered images of the microstructure as dark grey features, and distinguishable from the residual porosity. Samples prepared with excess La exhibited grains with La rich cores.

The thermoelectric properties of the samples shown in Fig. 9 are presented in Fig. 10. The electrical resistivities of the excess doped materials were significantly lower than the baseline L2 material (Fig. 10a). The resistivity of L2-5La and L2-10La samples are similar. Whilst La^{3+} substitution reduces the electrical resistivity compared to the baseline L2 material, there is no systematic trend for additions of La. In contrast, Nb substitution systematically improves electrical conductivity;
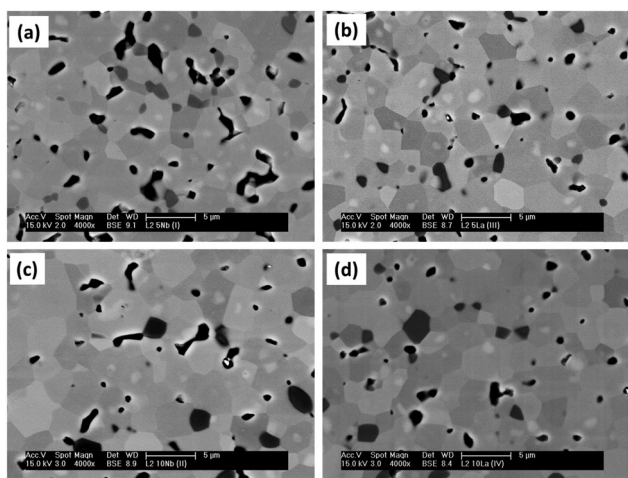
Fig. 9 Backscattered SEM images: (a) L2-5Nb; (b) L2-5La; (c) L2-10Nb; (d) L2-10La.

L2-10Nb has the lowest electrical resistivity of all the samples. The Seebeck coefficients of lanthanum-doped samples were marginally higher than for niobium-doped samples (Fig. 10b); values for all the samples range between -50 μV K^{-1} at 300 K to -160 μV K^{-1} at 1000 K.

In the present study, the variation of thermal conductivity with excess doping was not significant, and only marginally different from the control sample. This can be attributed to the constant concentration of vacancies in the doped L2 samples, giving average thermal conductivities of 5 W m^{-1} K^{-1} to 3 W m^{-1} K^{-1} across the temperature range (Fig. 10c). It should

be noted that excess doping of lanthanum and niobium actually increases the total thermal conductivity due to an increase in electronic thermal conductivity.

The temperature dependence of *ZT* for these samples is presented in Fig. 10d. The use of excess La and Nb has been beneficial; the *ZT* values for all the doped samples are higher than for the baseline L2 material, which had a maximum *ZT* value of 0.25. Samples prepared with 10% excess Nb had *ZT* values of 0.32 at 1000 K, whilst samples prepared with 5% excess La exhibited the highest *ZT* values of 0.345 at 1000 K. Clearly, the generation of additional charge carriers, through the combination of both reducing sintering conditions and excess doping by La or Nb, is a particularly effective strategy for improving the performance or SrTiO$_3$-based thermoelectric materials. Although the overall figure of merit for La and Nb doped samples are not significantly different, the values for both are significantly higher than for the baseline L2 – 24 hours Ar/5%H$_2$ sample. Indeed, a selective approach can be employed to enhance thermoelectric properties. Firstly, the carrier concentration can be increased, and then independently the charge mobility can be improved by modifying the grain boundary resistance and the effective carrier mass $\left(\dfrac{m^*}{n^{\frac{2}{3}}}\right)$ without affecting carrier concentration. One example of the latter approach was highlighted in the work of Wang *et al.* on yttria-stabilised zirconia nano-inclusions in Nb-doped SrTiO$_3$.[23] However, the present work demonstrates unambiguously the relative contributions from the two strategies based on vacancy concentrations and carrier concentrations.
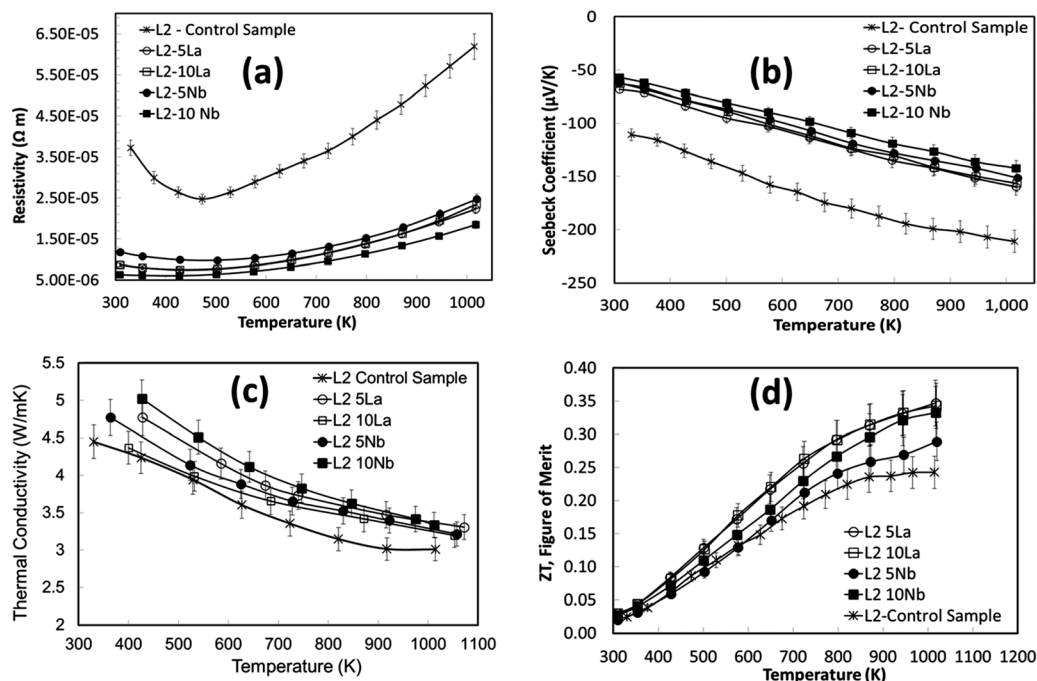

Fig. 10 Temperature dependence of thermoelectric properties for doped L2 samples sintered under reducing conditions: (a) resistivity; (b) Seebeck coefficient; (c) thermal conductivity; (d) figure of merit. Key for symbols: $\times$ – base L2 composition; $\bullet$ – L2 5Nb; $\blacksquare$ – L2 10Nb; $\bigcirc$ – L2 5La; $\square$ – L2 10 La.

26484 | *Phys. Chem. Chem. Phys.*, 2016, **18**, 26475–26486

This journal is © the Owner Societies 2016

Conclusions

High quality $Sr_{0.8}La_{0.067}Ti_{0.8}Nb_{0.2}O_{3-\delta}$ ceramics were prepared under reducing conditions. The presence of 20 mole% $La_{1/3}NbO_3$ in the $SrTiO_3$ base material generates $\sim 13\%$ vacancies on the A-sites; this fraction was fixed across all compositions. The physical properties, microstructure and thermoelectric properties were highly dependent on the sintering conditions, reflecting changes in defect concentrations and second phase development. Grain sizes were typically 7–10 μm where sintered in reducing conditions, but ~ 13 μm when sintered in air. The materials exhibited a simple cubic structure ($Pm\bar{3}m$ space group) which did not change with processing conditions. However, as samples were sintered for increasing time under reducing conditions there were increasing amounts of a $Ti_{1-x}Nb_xO_{2-y}$ second phase, as well as the formation of core–shell structures. Both helped to reduce thermal conductivity.

TEM investigations confirmed the cubic symmetry and revealed a high density of dislocations and linear imperfections within the grains. STEM-EELS and STEM-EDXS investigations at atomic resolution demonstrated conclusively a uniform distribution of La, Nb and cation vacancies within the lattice, with no evidence of any ordering or superlattice structures. The presence of $\sim 13\%$ A-site vacancies helps to reduce the electrical resistivity by approximately 50% compared to (undoped) $SrTiO_3$. Processing under reducing conditions led to oxygen deficiencies. XPS and thermogravimetry demonstrated an oxygen deficiency, $\delta = 0.082$ for the samples sintered for 24 hours. The resulting increase in carrier concentration (three orders of magnitude compared to air-sintered samples) and approximate doubling of the carrier mobility significantly improved the power factor, and led to a thermoelectric figure of merit (ZT) of 0.25 at 1000 K.

Further systematic improvement in thermoelectric properties was achieved by selective doping by lanthanum and niobium. By using up to 10% excess La or Nb it was possible to generate additional charge carriers, while maintaining a constant concentration of A-site vacancies. Grain sizes were much smaller (<5 μm) and there was still evidence of the $Ti_{1-x}Nb_xO_{2-y}$ second phase. The presence of additional charge carriers reduced the electrical resistivity by up to one order of magnitude. In contrast, the additional carriers marginally increased thermal conductivity as the extra La or Nb increased the electronic component of thermal conductivity. As a result, high values of ZT of 0.25 to 0.345 were achieved at 700 to 1000 K. Further improvements should be possible by improving the carrier concentrations and mobility, and by reducing grain boundary resistance while maintaining similar A-site vacancy concentrations. Nevertheless, the present work demonstrates unambiguously the relative contributions from the two strategies based on vacancy concentrations and carrier concentrations.

Acknowledgements

References

1 T. M. Tritt, *Annu. Rev. Mater. Res.*, 2011, **41**, 433–448.
2 D. M. Rowe, *Thermoelectrics handbook macro to nano*, CRC Press, Boca Raton, 2006.
3 J. W. Fergus, *J. Eur. Ceram. Soc.*, 2012, **32**, 525–540.
4 G. J. Snyder and E. S. Toberer, *Nat. Mater.*, 2008, **7**, 105–114.
5 W. S. Choi, H. Ohta, S. J. Moon, Y. S. Lee and T. W. Noh, *Phys. Rev. B: Condens. Matter Mater. Phys.*, 2010, **82**, 024301.
6 W. S. Choi, H. K. Yoo and H. Ohta, *Adv. Funct. Mater.*, 2015, **25**, 799–804.
7 I. Terasaki, Y. Sasago and K. Uchinokura, *Phys. Rev. B: Condens. Matter Mater. Phys.*, 1997, **56**, 12685–12687.
8 K. Koumoto, Y. F. Wang, R. Z. Zhang, A. Kosuga and R. Funahashi, *Annu. Rev. Mater. Res.*, 2010, **40**, 363–394.
9 G. K. Ren, J. L. Lan, C. C. Zeng, Y. C. Liu, B. Zhan, S. Butt, Y. H. Lin and C. W. Nan, *JOM*, 2015, **67**, 211–221.
10 W. S. Liu, Q. Jie, H. S. Kim and Z. F. Ren, *Acta Mater.*, 2015, **87**, 357–376.
11 L. Bocher, M. H. Aguirre, D. Logvinovich, A. Shkabko, R. Robert, M. Trottmann and A. Weidenkaff, *Inorg. Chem.*, 2008, **47**, 8077–8085.
12 M. Molinari, D. A. Tompsett, S. C. Parker, F. Azough and R. Freer, *J. Mater. Chem. A*, 2014, **2**, 14109–14117.
13 D. Srivastava, F. Azough, R. Freer, E. Combe, R. Funahashi, D. M. Kepaptsoglou, Q. M. Ramasse, M. Molinari, S. R. Yeandel, J. D. Barand and S. C. Parker, *J. Mater. Chem. C*, 2015, **3**, 12245–12259.
14 H. Ohta, K. Sugiura and K. Koumoto, *Inorg. Chem.*, 2008, **47**, 8429–8436.
15 H. Ohta, S. Kim, Y. Mune, T. Mizoguchi, K. Nomura, S. Ohta, T. Nomura, Y. Nakanishi, Y. Ikuhara, M. Hirano, H. Hosono and K. Koumoto, *Nat. Mater.*, 2007, **6**, 129–134.
16 J. Ravichandran, W. Siemons, D. W. Oh, J. T. Kardel, A. Chari, H. Heijmerikx, M. L. Scullin, A. Majumdar, R. Ramesh and D. G. Cahill, *Phys. Rev. B: Condens. Matter Mater. Phys.*, 2010, **82**, 165126.
17 T. Okuda, K. Nakanishi, S. Miyasaka and Y. Tokura, *Phys. Rev. B: Condens. Matter Mater. Phys.*, 2001, **63**, 113104.
18 H. Muta, K. Kurosaki and S. Yamanaka, *J. Alloys Compd.*, 2005, **392**, 306–309.
19 S. Ohta, H. Ohta and K. Koumoto, *J. Ceram. Soc. Jpn.*, 2006, **114**, 102–105.
20 K. Kato, M. Yamamoto, S. Ohta, H. Muta, K. Kurosaki, S. Yamanaka, H. Iwasaki, H. Ohta and K. Koumoto, *J. Appl. Phys.*, 2007, **102**, 116107.
21 W. Wunderlich, H. Ohta and K. Koumoto, *Phys. B*, 2009, **404**, 2202–2212.

22 J. Liu, C. L. Wang, W. B. Su, H. C. Wang, P. Zheng, J. C. Li, J. L. Zhang and L. M. Mei, *Appl. Phys. Lett.*, 2009, **95**, 162110.

23 W. H. Gong, H. Yun, Y. B. Ning, J. E. Greedan, W. R. Datars and C. V. Stager, *J. Solid State Chem.*, 1991, **90**, 320–330.

24 S. R. Popuri, A. J. M. Scott, R. A. Downie, M. A. Hall, E. Suard, R. Decourt, M. Pollet and J. W. G. Bos, *RSC Adv.*, 2014, **4**, 33720–33723.

25 Z. L. Lu, H. R. Zhang, W. Lei, D. C. Sinclair and I. M. Reaney, *Chem. Mater.*, 2016, **28**, 925–935.

26 D. Neagu and J. T. S. Irvine, *Chem. Mater.*, 2011, **23**, 1607–1617.

27 K. Park, J. S. Son, S. I. Woo, K. Shin, M. W. Oh, S. D. Park and T. Hyeon, *J. Mater. Chem. A*, 2014, **2**, 4217–4224.

28 J. Liu, C. L. Wang, H. Peng, W. B. Su, H. C. Wang, J. C. Li, J. L. Zhang and L. M. Mei, *J. Electron. Mater.*, 2012, **41**, 3073–3076.

29 A. V. Kovalevsky, A. A. Yaremchenko, S. Populoh, P. Thiel, D. P. Fagg, A. Weidenkaff and J. R. Frade, *Phys. Chem. Chem. Phys.*, 2014, **16**, 26946–26954.

30 T. Teranishi, Y. Ishikawa, H. Hayashi, A. Kishimoto, M. Katayama and Y. Inada, *J. Am. Ceram. Soc.*, 2013, **96**, 2852–2856.

31 H. C. Wang, C. L. Wang, W. B. Su, J. Liu, H. Peng, J. L. Zhang, M. L. Zhao, J. C. Li, N. Yin and L. M. Mei, *J. Alloys Compd.*, 2009, **486**, 693–696.

32 A. M. Dehkordi, S. Bhattacharya, T. Darroudi, J. W. Graff, U. Schwingenschlogl, H. N. Alshareef and T. M. Tritt, *Chem. Mater.*, 2014, **26**, 2478–2485.

33 A. M. Dehkordi, S. Bhattacharya, J. He, H. N. Alshareef and T. M. Tritt, *Appl. Phys. Lett.*, 2014, **104**, 193902.

34 C. Chen, T. S. Zhang, R. Donelson, T. T. Tan and S. Li, *J. Alloys Compd.*, 2015, **629**, 49–54.

35 H. Muta, K. Kurosaki and S. Yamanaka, *J. Alloys Compd.*, 2003, **350**, 292–295.

36 A. I. Abutaha, S. R. S. Kumar, K. Li, A. M. Dehkordi, T. M. Tritt and H. N. Ashareef, *Chem. Mater.*, 2015, **27**, 2165–2171.

37 A. V. Kovalevsky, S. Populoh, S. G. Patricio, P. Thiel, M. C. Ferro, D. P. Fagg, J. R. Frade and A. Weidenkaff, *J. Phys. Chem. C*, 2015, **119**, 4466–4478.

38 A. V. Kovalevsky, A. A. Yaremchenko, S. Populoh, A. Weidenkaff and J. R. Frade, *J. Phys. Chem. C*, 2014, **118**, 4596–4606.

39 A. A. Yaremchenko, S. Populoh, S. G. Patricio, J. Macias, P. Thiel, D. P. Fagg, A. Weidenkaff, J. R. Frade and A. V. Kovalevsky, *Chem. Mater.*, 2015, **27**, 4995–5006.

40 M. Backhaus-Ricoult, J. R. Rustad, D. Vargheese, I. Dutta and K. Work, *J. Electron. Mater.*, 2012, **41**, 1636–1647.

41 Y. F. Wang, C. L. Wan, X. Y. Zhang, L. M. Shen, K. Koumoto, A. Gupta and N. Z. Bao, *Appl. Phys. Lett.*, 2013, **102**, 183905.

42 J. Liu, H. C. Wang, W. B. Su, C. L. Wang, J. L. Zhang and L. M. Mei, *Solid State Sci.*, 2010, **12**, 134–137.

43 T. Shoji, S. Sugiyama and K. Fuda, *Mater. Trans.*, 2011, **52**, 1531–1534.

44 D. Srivastava, F. Azough, M. Molinari, S. C. Parker and R. Freer, *J. Electron. Mater.*, 2015, **44**, 1803–1808.

45 H. M. Rietveld, *Acta Crystallogr.*, 1967, **22**, 151–152.

46 M. I. Mendelson, *J. Am. Ceram. Soc.*, 1969, **52**, 443–448.

47 R. Taylor, *J. Phys. E: Sci. Instrum.*, 1980, **13**, 1193–1199.

48 R. D. Cowan, *J. Appl. Phys.*, 1963, **34**, 926–930.

49 J. E. Daw, *Measurement of specific heat capacity using differential scanning calorimeter*, U.S. Department of Energy National Laboratory, Idaho, 2008.

50 L. Jones and P. D. Nellist, *Microsc. Microanal.*, 2013, **19**, 1050–1060.

51 C. Koch, PhD thesis, Arizona State University, 2002.

52 G. Lucas, P. Burdet, M. Cantoni and C. Hébert, *Micron*, 2013, **52–53**, 49–56.

53 S. A. Prosandeev, I. P. Raevski and M. A. Bunin, *Phys. Rev. B: Condens. Matter Mater. Phys.*, 2004, **70**, 157101.

54 K. Koumoto, Y. F. Wang, R. Z. Zhang, A. Kosuga and R. Funahashi, *Annu. Rev. Mater. Res.*, 2010, **40**, 363–394.

55 Z. Lu, H. Zhang, W. Lei, D. C. Sinclair and I. M. Reaney, *Chem. Mater.*, 2016, **28**, 925–935.

56 M. G. Sahini, J. R. Tolchard, K. Wiik and T. Grande, *Dalton Trans.*, 2015, **44**, 10875–10881.

57 T. Matsunaga and H. Saka, *Philos. Mag. Lett.*, 2000, **80**, 597–604.

58 S. B. Lee, W. Sigle, F. Phillipp and D. Brunner, *Acta Mater.*, 2005, **53**, 1843–1848.

59 S. J. Pennycook and P. D. Nellist, *Scanning transmission electron microscopy: imaging and analysis*, Springer Science & Business Media, 2011.

60 S. D. Findlay, N. Shibata, H. Sawada, E. Okunishi, Y. Kondo, T. Yamamoto and Y. Ikuhara, *Appl. Phys. Lett.*, 2009, **95**, 191913.

61 M. S. J. Marshall, D. T. Newell, D. J. Payne, R. G. Egdell and M. R. Castell, *Phys. Rev. B: Condens. Matter Mater. Phys.*, 2011, **83**, 35410.

62 NIST, *X-ray Photoelectron Spectroscopy Database*, Material Measurement Laboratory (MML), Gaithersburg, 2012.

63 P. Blennow, A. Hagen, K. K. Hansen, L. R. Wallenberg and M. Mogensen, *Solid State Ionics*, 2008, **179**, 2047–2058.

64 W. D. Kingery, *Introduction to ceramics*, John Wiley & Sons, 1960.

65 D. Neagu and J. T. S. Irvine, *Chem. Mater.*, 2010, **22**, 5042–5053.

66 Y. F. Wang, K. Fujinami, R. Z. Zhang, C. L. Wan, N. Wang, Y. S. Ba and K. Koumoto, *Appl. Phys. Express*, 2010, **3**, 31101.

67 H. Taguchi, M. Sonoda and M. Nagao, *J. Solid State Chem.*, 1998, **137**, 82–86.

68 M. Cutler, J. F. Leavy and R. L. Fitzpatrick, *Phys. Rev.*, 1964, **133**, 1143–1152.

69 S. Ohta, T. Nomura, H. Ohta and K. Koumoto, *J. Appl. Phys.*, 2005, **97**, 34106.

26486 | *Phys. Chem. Chem. Phys.*, 2016, **18**, 26475–26486

This journal is © the Owner Societies 2016